AIChE

Hybrid PIV/PTV Measurements of Velocity and Position Distributions of Gas-Conveyed Particles in Small, Narrow Channels

Martin W. Korevaar, Johan T. Padding, Niels G. Deen, and J. A. M. (Hans) Kuipers
Multiphase Reactors Group, Dept. of Chemical Engineering and Chemistry, Eindhoven University of Technology,
5600 MB Eindhoven, The Netherlands

Jue Wang, Martin de Wit, and Maarten A. I. Schutyser
Laboratory of Food Process Engineering, Agrotechnology & Food Sciences, Wageningen University,
6700 AA Wageningen, The Netherlands

DOI 10.1002/aic.14928

Pneumatic conveying of particles is generally applied in large ducts. However, new applications are emerging which benefit from millimeter-sized ducts; for example, triboelectric separators where intensive wall-particle contact is desirable. An optical method is proposed to measure the distribution of the position and velocity of 100–1000 μm particles in such narrow ducts. Images of the system are captured using a digital camera on which a Hough transform is applied to detect the particles and their positions. The velocities are acquired by applying a hybrid particle tracking and particle image velocimetry approach. This made it is possible to overcome challenges caused by suboptimal lighting, nonsmooth background, and a large ratio between particle and duct diameter ($> \mathcal{O}(0.1)$). It is shown that the algorithm is subpixel accurate when sufficient particles can be sampled. Finally, typical results are shown to illustrate the method's capabilities. © 2015 American Institute of Chemical Engineers *AIChE J*, 61: 3616–3627, 2015
Keywords: particle image velocimetry, pneumatic conveying, millimeter ducts, two-phase flow

Introduction

Pneumatic conveying of particles is generally the preferred way of transporting particulate material and, therefore, an omnipresent technique in industry. As a consequence, it received a lot of attention in literature.[1–4] In general, ducts and tubes of large diameters are applied, to make the transport as energy efficient as possible. For that reason, ducts of smaller scale, with a diameter of a few millimeters or less, have not been extensively studied. However, new technologies and applications are arising for which transport through narrow channels is important. For example, it is important to understand pneumatic conveying through narrow ducts when tackling problems associated with sealing of underground gas drainage systems used in coal mining industry.[5] Other examples include applications where intensive wall-particle contact is desired, such as triboelectric separators.[6,7] In such systems, the electrostatic charging of particles due to particle-wall and particle-particle contact is used to separate powder mixtures. The driving force in the separation is then the difference in polarity and charge-per-mass that different materials acquire when colliding with the wall. As this method uses no water, it can become an important and energy efficient alternative for currently widely applied wet separation of many food ingredients, toward a more sustainable food producing future.[8–12] With these new emerging applications of pneumatic conveying in narrow ducts, investigations of the behavior of these systems is important in order to achieve optimal design.

When studying pneumatic conveying systems, two quantities are of primary interest: the particle positions and the particle velocities. Nowadays, a wide variety of noninvasive techniques exist to acquire these quantities.[13] In millimeter-sized pneumatic conveying systems the particle velocities can reach 10 m/s or more, while at the same time particle sizes reach below 100 μm. Only optical methods have sufficient temporal and spatial resolution to capture such small, fast moving particles. The drawback of optical methods is the need for optical accessibility, which puts a constraint on the wall material while this can be an important system property. This is the case in triboelectric separators where the wall material strongly determines the charging of the powder and thus its separation efficiency.[10,14–16]

Despite the high spatial and temporal resolution of optical methods, imaging small systems with high particle velocities is still challenging because the magnification is necessarily large and the exposure time short. In the field of micro particle image velocimetry (PIV) and particle tracking velocimetry (PTV), even smaller fields of view (FOV) have been studied with even less light.[17] There the problem of lighting has been tackled using laser instead of LED lighting at the cost of longer interframe time. This way, even high velocities (>15 m/s) can be measured accurately (e.g., in Fiscaletti et al.[18]). Another approach to achieve better measurements is to use particle shadow velocimetry.[19] Drawback is that this imposes

---

Correspondence concerning this article should be addressed to J. T. Padding at J.T.Padding@tue.nl.

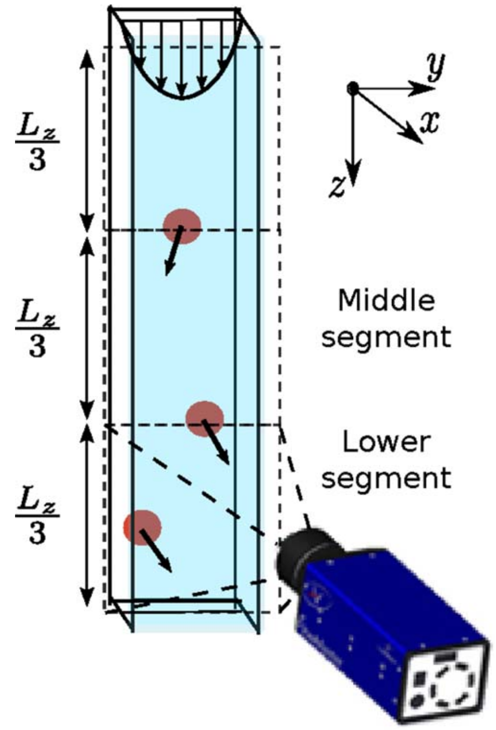

Figure 1. A schematic of the experimental setup as used for the experiments described in this article.

Particles and gas are introduced at the top, particles hit the walls while traveling through the duct and exit at the bottom. Three segments can be distinguished; all measurements were performed on the middle and lower section. The cover is transparent which enables the camera to capture the particles. The dimensions of the duct in *x*, *y*, and *z* direction are indicated in Table 1. [Color figure can be viewed in the online issue, which is available at wileyonlinelibrary.com.]

a restriction on the material of the back wall as well. This is undesirable when the material itself is of importance, as explained above. Furthermore, such adaptations of an experimental setup are not always feasible.

Both PIV and PTV have originally been developed to visualize the flow of a fluid. However, they have also been successfully applied to visualize the velocity of a particulate phase in a two-phase system. To select whether PIV or PTV is the best choice, the source density N_S is of importance.[20,21] It is defined as the number of particles

$$N_S = \rho^{\#}\,\Delta z \frac{\pi}{4} D_{p,\mathrm{im}}^2 M^{-2} \tag{1}$$

with $\rho^{\#}$ the mean number of visible particles per unit volume, Δz the depth of the FOV (focus depth of field), $D_{p,\mathrm{im}}$ the diameter of the particle image (in pixels), and M the image magnification (in pixels per meter). When the particle's true diameter is much larger than the wavelength of light, then $D_{p,\mathrm{im}}/M \approx D_p$ (in m). Furthermore, the number density can be written in terms of the solids volume fraction, ε_s and particle diameter D_p using $\rho^{\#} = 6\varepsilon_s / \left(\pi D_p^3\right)$. Substituting this in Eq. 1 yields

$$N_S = \frac{3\varepsilon_s \,\Delta z}{2D_p} \tag{2}$$

Following Ref. 20, one should use PTV when $N_S \ll 1$ while PIV is preferred when $N_S = \mathcal{O}(1)$. For dilute pneumatic conveying systems, $\varepsilon_s \leq 0.01$; when looking at ducts with diameters of a few millimeters with a macrolens, the limited depth of field gives typically $\Delta z \leq \mathcal{O}\left(10^{-3}\right)$ m. Consequently, when particles of a hundred micrometer are considered, $N_S \leq 0.1$. This is in the transition regime where neither PIV nor PTV is *a priori* favorable.

In case PIV is chosen, the interrogation area should be the size of a few particle diameters. However, in the case of narrow ducts this can be a problem when the duct diameter consists of only a few particle diameters, because this will allow for only a very low spatial resolution of particle velocity vectors over the width of the duct. This is undesirable if velocity profiles over the width are of interest. In case PTV is the method of choice, the velocities of individual particles are determined. This enables in principle a very high resolution of the average particle velocity profile over the channel width, provided that sufficient particles pass the FOV. However, a drawback of PTV is that it relies heavily on the detection of particles in order to determine their velocity. Consequently, in images where the particle segmentation is difficult this is not the preferred method as it will yield erroneous velocities at places where segmentation fails. As a matter of fact, this is generally the case for smaller systems where lighting is a problem and where small imperfections in the front cover or back wall are prominently visible due to the large magnification. These imperfections occur even when great care is taken during manufacturing or handling of the duct. Consequently, PTV can also not be applied directly to determine the average velocity of pneumatically conveyed powders in a small channel.

Therefore, in this work we propose to use a combined approach of PIV and PTV to exploit both their merits without suffering from their drawbacks. In our approach, we determine the velocities independent of the segmentation results, while maintaining a high resolution of the velocity profile over the width of the channel, even when the duct to particle diameter ratio is smaller then 10. We validate this new technique on artificial images and therefore extensively asses its accuracy. Furthermore, we apply the method to images of a real triboelectric separator with a millimeter-sized duct using front lighting with LED lights. Typical result will be shown to illustrate the method's capacity.

Methods

Experimental setup

An experimental setup has been built at Wageningen University, to investigate the charging behavior of materials as well as their separation potential. In this article, we focus on the charging duct. This is the part of the setup where the particles acquire charge while they are pneumatically conveyed, as schematically represented in Figure 1. The setup is able to dose the powder mass rate accurately between 139 and 694 mg/s. In this work, we focus on a mass rate of $\dot{m} = 694$ mg/s. Polystyrene particles with an average diameter of 400 μm are fed at the top of the charging duct and will attain charge while traveling through the duct as they hit the walls. They enter the duct together with cocurrently fed gas; the flow rate of the gas can be altered independently of the particle mass rate. In this work, the gas flow rate has been set such that the superficial gas velocity in the duct is 2.5, 8, or 15 m/s, respectively. The walls of the duct are made of aluminum, except for the cover which is made of transparent poly(methyl methacrylate). Consequently, the charging slit is noninvasively but optically accessible, enabling high

Table 1. Overview of Experimental Parameters

Quantity	Value	Unit
Gas and duct		
$\bar{v}_{bg}$	2.5, 8 and 15	m s^{-1}
L_x	2.5×10^{-3}	m
L_y	3.0×10^{-3}	m
L_z	0.22	m
Polystyrene particles		
$\dot{m}$	6.94×10^{-4}	kg s^{-1}
ρ_p	1050	kg m^{-3}
D_p	400×10^{-6}	m

speed and high resolution images acquisition from which particle velocity and positions can be determined. To be able to detect the particles using digital image analysis (DIA), the particles should cover sufficient pixels on the camera's SMOS sensor. The camera used in this work is LaVision's Imager pro HS 4M in combination with their software Davis. A 200 mm Nikon f/4 macrolens was applied and positioned at about 0.55 m from the duct, resulting in an image of about 14 pixels per particle diameter. It turned out that the whole depth of the duct could be sufficiently captured within the field of focus, despite the large magnification and fully opened aperture (f/4). To image the particles without too much motion blur, a sufficiently short exposure time needs to be set. It was found that for the chosen gas velocity of 2.5, 8, and 15 m/s, an exposure time of, respectively, 70, 45, and 30 μs suffices. The duct was lighted with two LED lights, positioned left and right of the camera. This induces two glare points in each particle. This turns out to be favorable for the determination of the velocity, as will be explained in subsection on particle velocity. Finally, to illustrate the development of the particle position and velocity with streamwise position, all measurements were performed at a segment in the middle as well as at the bottom of the duct. The parameters of the experiments are summarized in Table 1.

Particle position

The positions of the particles are extracted from the images by DIA. The *imfindcircle* function from MATLAB's Image Processing toolbox is used to detect (segment) the particles. This function processes the image with an edge filter on which result the Hough transfer for circles is applied. The Hough transfer basically matches for every pixel how well the surrounding of the image looks like a circle of certain radius. If it matches well enough it is considered a circle. For full details on the algorithm, we refer to Refs. 22 and [23] or MATLAB's (online) help. The algorithm could detect the particles position and radius within one pixel accurate, that is, 1/15-th of the particle diameter. So if a particle is detected by the algorithm, its position is detected accurately within one pixel. However, sometimes a particle was not detected at all (false negative) or a feature in the background was erroneously detected as a particle (false positive). The influence of the false positives and negatives on the algorithm's accuracy is assessed in the following.

Accuracy. An important input parameter of the MATLAB function *imfindcircle* is the sensitivity parameter which determines whether some feature in the image resembles a circle sufficiently. Setting it too low will yield false negatives, setting it too high will yield false positives. To asses the accuracy of the detection algorithm and influence of this "sensitivity" parameter, its results need to be compared to a so called ground truth. In this work, we choose to derive such a ground truth, by selecting the particles manually. The results of the segmentation algorithm are compared to this ground truth for different settings of the sensitivity parameter. From this we derived which particles are determined correctly as particles, that is, the true positives, as well as the false positives and false negatives. In Figure 2, the false positives and negatives are shown as function of their position between the two walls. This illustrates that as long as the parameter is set between 0.87 and 0.9, most particles are detected (only few false negatives) and also most detected particles are actual particles (only few false positives). Moreover, the false negatives and false positives do not show any bias to the lateral position (y-position) using that setting. This shows that the results of the algorithm are reliable. However, it should be noted that the above procedure was only done for one measurement and for only ten frames, as it is very time consuming. It may be

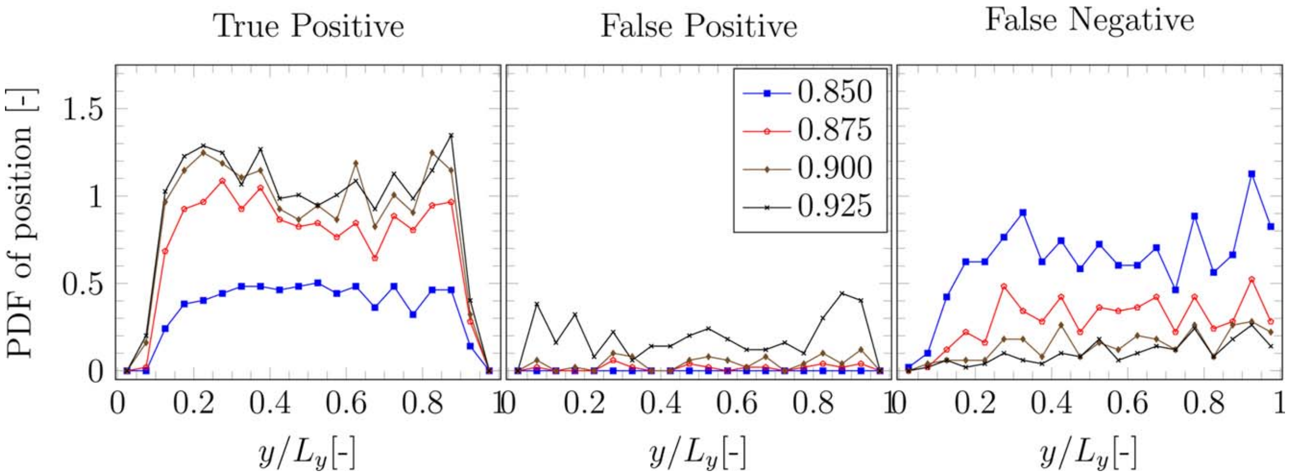

Figure 2. The accuracy of the algorithm in comparison with a manually selected ground truth.

For all figures, the number of detected particles is shown as function of the lateral (y-) position and shows the results for different settings of the sensitivity parameter. The number of detected particles is normalized to the total number of ground truth particles divided by the bin width. The left figure shows the number of detected particles that are actual particles (true positives). The middle figure shows the detected particles that are not really particles (false positives). The right figure shows the particles that the algorithm failed to detect (false negatives). For this assessment, 10 frames with on average 100 particles have been used. [Color figure can be viewed in the online issue, which is available at wileyonlinelibrary.com.]

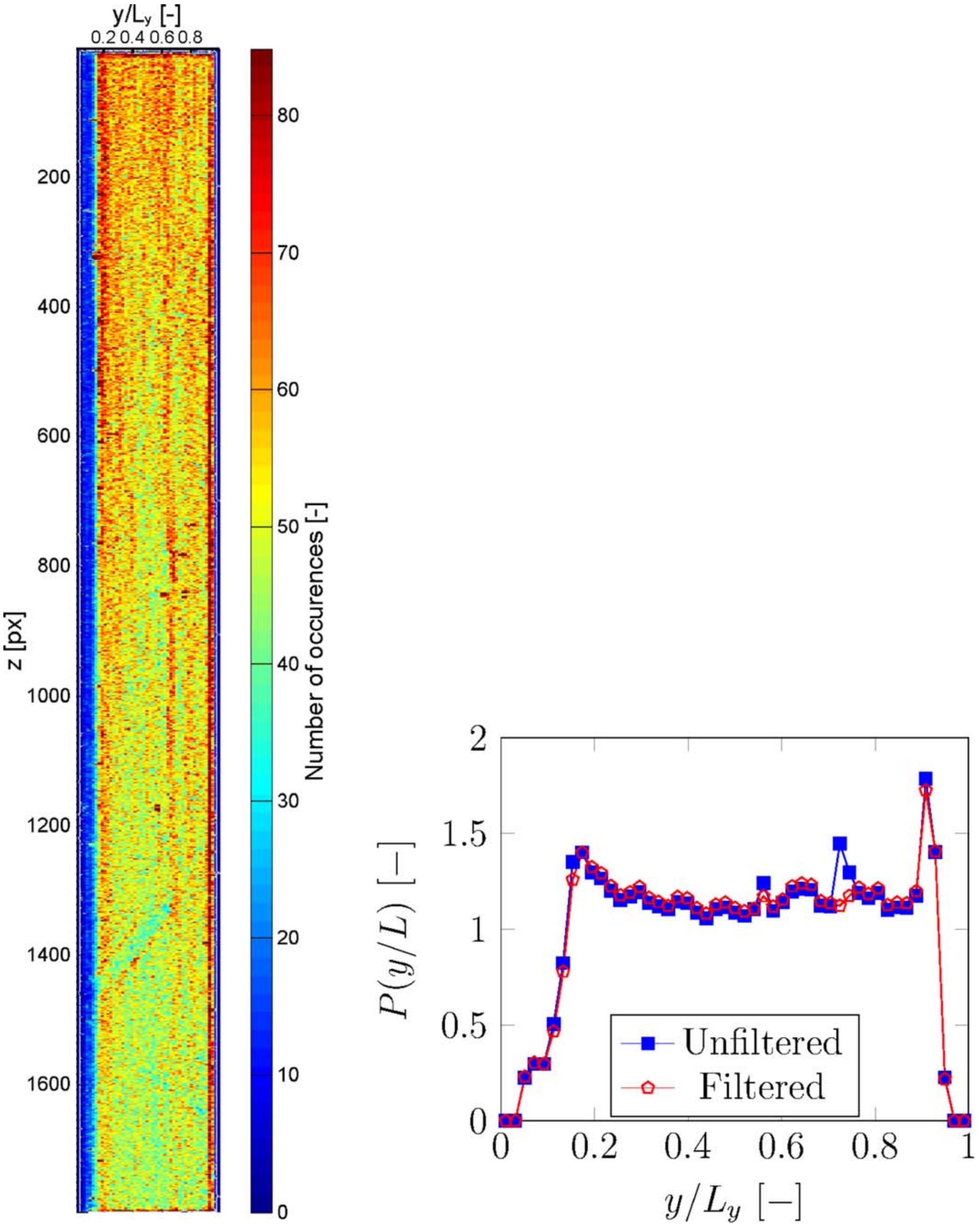

Figure 3. Left: The 2-D histograms of the occurrence of particles at a certain *y*, *z* position. Where *z* is the streamwise direction and *y* the lateral direction. Right: PDF of the position between the two walls with and without filtering of the data. Note that this is the projection on the *y* axis of the left figure and how the peak at $y = 0.7$ is removed due to filtering.

[Color figure can be viewed in the online issue, which is available at wileyonlinelibrary.com.]

possible that for different measurements with, for example, different exposure times, this is different. For the remainder, we assume it is not. As a matter of fact, it was observed that for denser flow, both the number of false positives and false negatives decreased relative to the number of true positives.

When the particle positions are detected, a two-dimensional (2-D) histogram of their occurrences at certain (y, z)-position can be determined. An example is shown in the left figure of Figure 3. Note how at some positions very high occurrences are found. They can be recognized by the dark red spots at, for example, $y = 0.5$ and $z = 850$ or $z = 1200$. These are caused by some features in the background, like a scratch in the back plate, instead of particles. As these are obvious false positives with an occurrence of more than 10 times more than the surrounding bins, they are filtered out. In Figure 3, this filter is demonstrated. A peak at $y = 0.7$ is visible for the unfiltered data, but it disappeared for the filtered data while they are the same for all other value of y. In the 2-D histogram, some features are visible, for example, a vertical red line structure at $y \approx 0.7$ or a diagonal blue line at $0 < y < 0.75$ and $1300 < z < 1450$. By projecting the 2-D image to the y axis, these features are averaged out and therefore no longer visible in Figure 3. This makes the one-dimensional (1-D) probability density function (PDF) robust to local false positives and negatives.

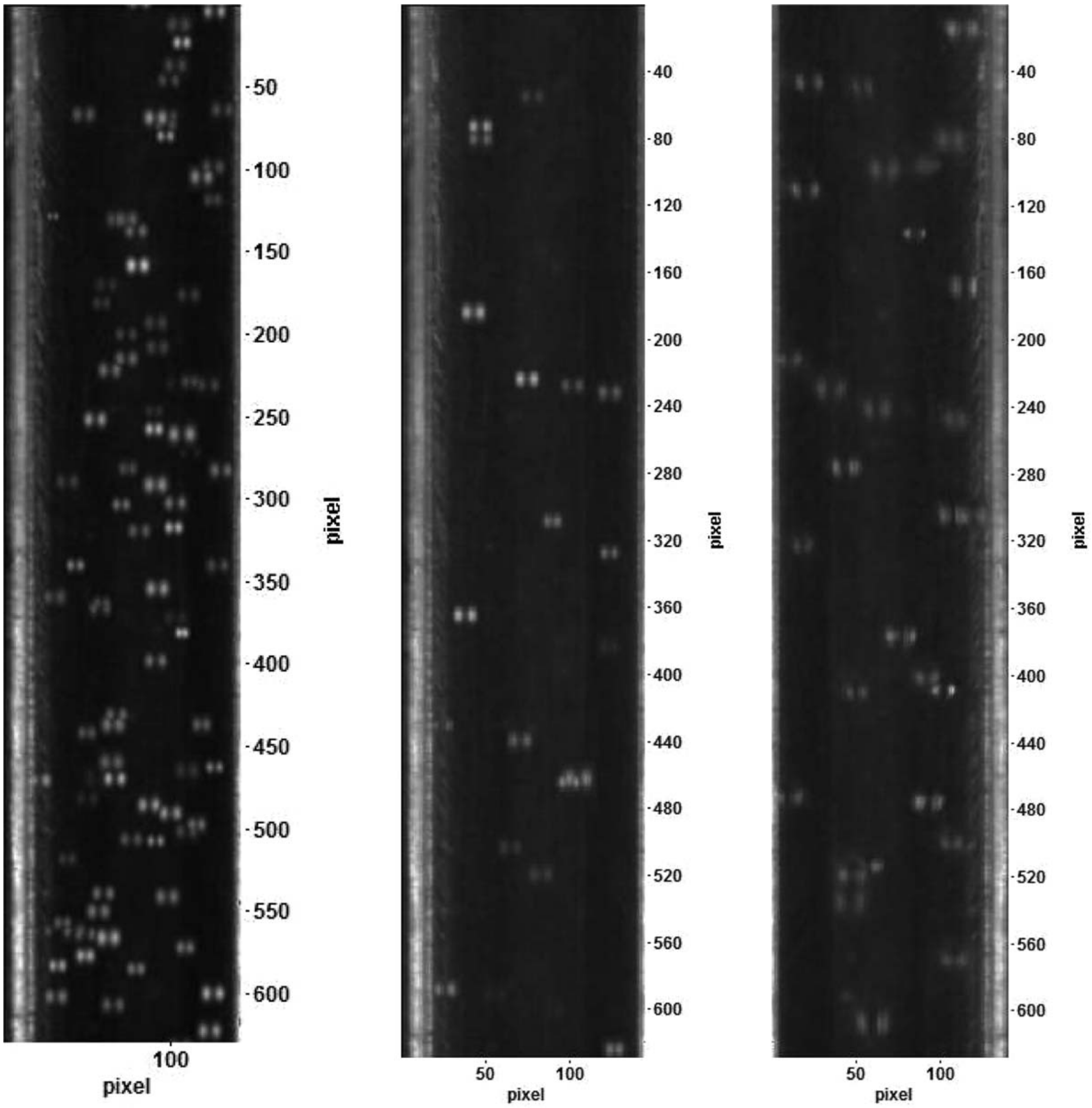

Figure 4. Artificial image with 100 particles per frame (left), with 20 particles (middle) and a real image with 20 particles per frame (right).

Particle velocity

To determine the velocity of the particles, the PIV algorithm of LaVisions software *Davis* is used. PIV is a classic experimental technique with which the velocity field of a fluid can be determined. This is achieved by acquiring frames of the fluid in which tracer particles are suspended. Each frame is subdivided in so-called interrogation areas; the average interframe displacement of all particles inside the interrogation area is determined by performing pattern matching on the two frames (through a cross-correlation). This leads to the average velocity of the particles ensemble. In a two-phase system, not the velocity of the fluid but of the particulate phase can be of interest. For both cases however, it holds that sufficient particles should reside in the interrogation area to have a sufficiently accurate velocity estimate. Consequently, the interrogation area should be sufficiently large. As a rule of thumb, an interrogation area should have size of about five particle diameters. However, the duct used in this work is only about seven particle diameters wide, resulting in a very poor resolution over the channel's width. Therefore, in this study it is chosen to have an interrogation area of one particle diameter instead. In this case, pattern matching will not be performed on an ensemble of particles, but rather on the (ensemble) of features of one particles. In the right image of Figure 4, an example of a captured image is shown. It is clear that particles cannot be recognized only by their contour, but also by two glare points. As both these glare points are bright, the PIV estimate is based on their displacement instead of the displacement of the one particle residing in the interrogation area. Moreover, these two glare points maintain their relative distance among different frames. This should both improve the displacement estimate of the PIV algorithm.

The Davis software itself cannot detect where the particles are. Therefore, the positions of the particles determined by the aforementioned MATLAB script are used. In this way, only the velocity from the interrogation areas that belong to a particle are used to determine particle velocities. The results of the remaining interrogation areas are neglected. It turned out that

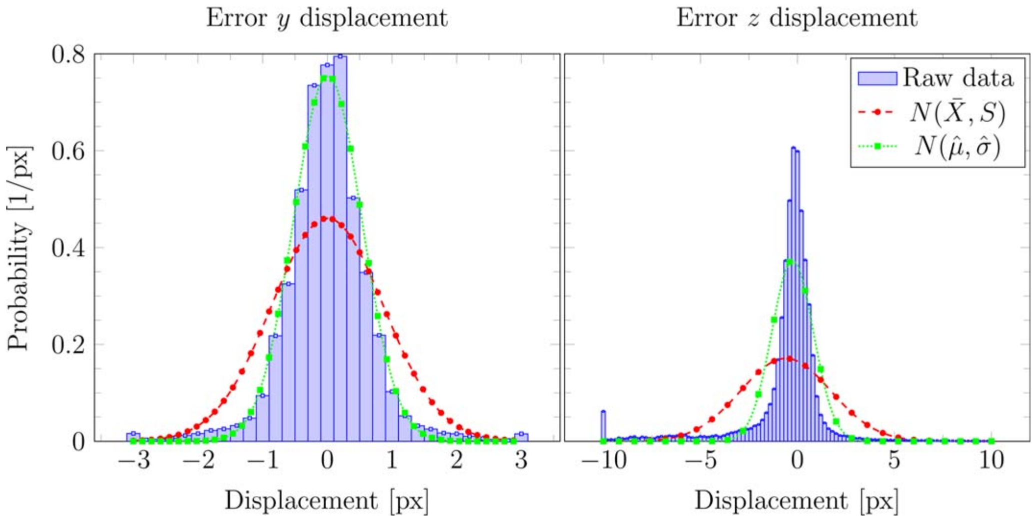

Figure 5. The distribution of the error for the displacement in *y* (left) and *z* direction (right).

The bars indicate the normalized histogram of the actual errors. The red line indicates the normal distribution with sample mean and standard deviation. The green line indicates the normal distribution with the mean and standard deviation of only the data that falls within $\bar{X} \pm 2S$. [Color figure can be viewed in the online issue, which is available at wileyonlinelibrary.com.]

Table 2. Overview of Distribution of the Particle Displacement Error

N_f	N	Direction	$\bar{X}$	S	$\hat{\mu}$	$\hat{\sigma}$	$\hat{\sigma}_\mu = \hat{\sigma}/\sqrt{N}$
20	23,000	Y	0.002	0.87	0.007	0.5	3×10^{-3}
		Z	−0.605	2.33	−0.25	1.1	7×10^{-3}
100	23,000	Y	−0.000	1.12	−0.004	0.7	5×10^{-3}
		Z	−0.361	2.72	−0.20	1.8	12×10^{-3}

N_f is the typical number of particles per frame and N is the total number of sampled particles. $\bar{X}$ and S are the average and standard deviation of the distribution of displacement errors, while $\hat{\mu}$ and $\hat{\sigma}$ are estimates of the average and standard deviation after filtering out outliers (see main text for details). The last column shows the estimated error $\hat{\sigma}_\mu$ in the mean displacement. All values are in pixels.

using the interrogation area closest to the center of the particle, gives the best estimate for the actual velocity of the particle.

As this is not a standard way of using PIV, we rather refer to this as a hybrid PIV-PTV method. To show that this is a valid way of determining the particle velocity, validation has been done using artificial images. The radii of the particles are drawn from a distribution as determined from particles in real images. The same holds for the intensity of the glare points and the velocity of the particles. These artificial images of particles are added to an image of an empty duct to add realistic features such as scratches and dust to really challenge the algorithm. An example of an artificial and a real image are shown in Figure 4.

By comparing the imposed velocity to the velocity determined by our hybrid PIV-PTV algorithm, the exact error can be assessed. In Figure 5, the distribution of the error is shown for both lateral and streamwise directions. The error in both directions seems to be normally distributed with some outliers,

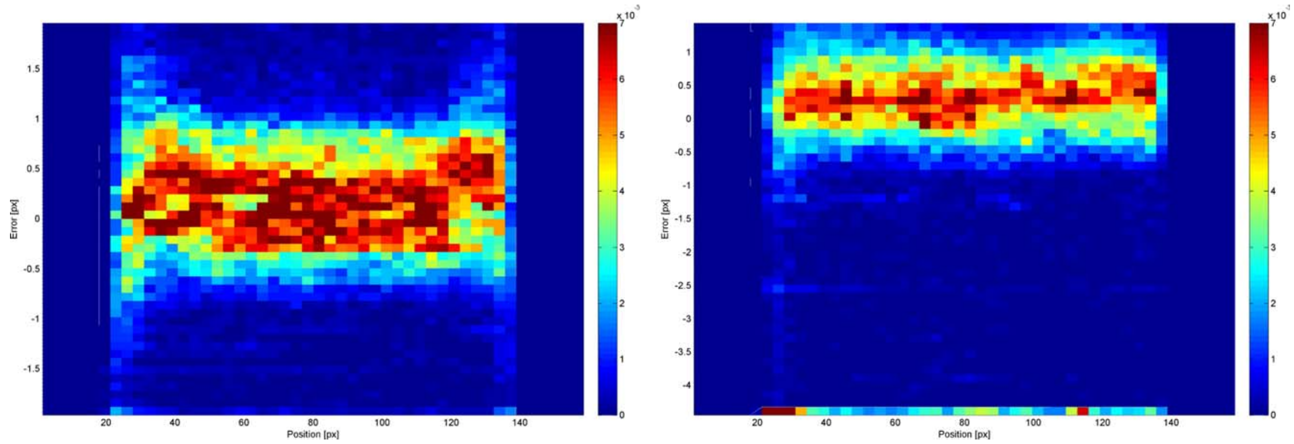

Figure 6. The distribution of the error of *y*-displacement (left) and *z*-displacement (right) as a function of the *y*-position.

Results for artificial images with 20 particles per frame. The left and right walls are located at 20 and 140 px, respectively. [Color figure can be viewed in the online issue, which is available at wileyonlinelibrary.com.]

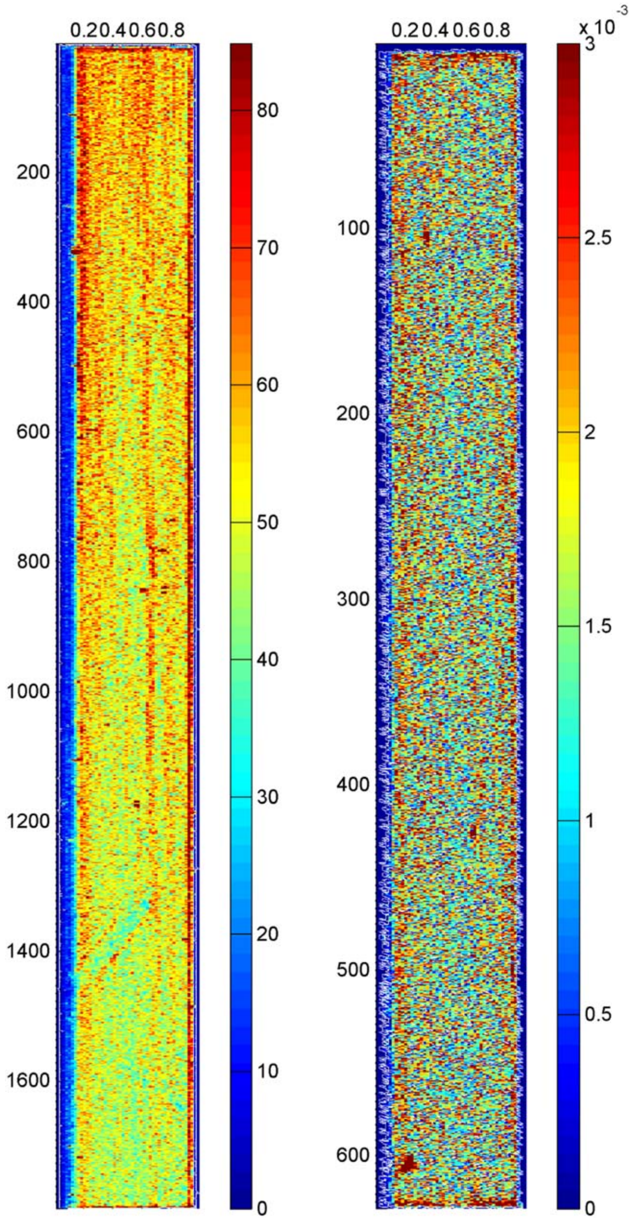

Figure 7. Examples of 2-D histograms of the occurrence of particles at a certain *y*, *z* position.

Here *z* is the streamwise direction and *y* the lateral direction. Histograms are determined from the middle section (left) and the bottom section (right). [Color figure can be viewed in the online issue, which is available at wileyonlinelibrary.com.]

especially for the streamwise velocity component. Most importantly, the distribution has a mean of approximately 0. As a consequence, by averaging over an increasing amount of individual particle velocity measurements at a specific location, an increasingly accurate estimate can be made of the average particle velocity at that location. The error in such an average velocity measurement can be derived from the distribution of the error for the displacement. We will now discuss this in detail.

When one tries to determine an estimator $\hat{\mu}$ and $\hat{\sigma}$ for the actual mean (μ) and standard deviation (σ) one could use the sample mean ($\bar{X}$) and standard deviation (S). However, in this case a very wide distribution is found which does not represents the data very well (red line). This is caused by the outliers as they weigh disproportionately heavy on particularly the standard deviation. These outliers can be removed by calculating the statistics deviation on a subset of the sample, that is all data that falls within $\bar{X} \pm 2S$; the mean and standard deviation of these subsets are referred to as $\bar{X}_{2S}$ and S_{2S}, respectively. The corresponding distribution is also plotted in Figure 5 by the green line which is indeed a better description of the sample distribution. In all cases, the outliers consist of less than 5% of the data. Thus, the estimators are given as

$$\hat{\mu} = \bar{X}_{2S} \quad \text{and} \quad \hat{\sigma} = S_{2S} \tag{3}$$

The values of the statistics are shown in Table 2; note how the accuracy is barely influenced by the number density. The typical displacement of the particles in y and z direction is typically 1 and 10 pixels/frame, respectively. This makes the individual particle displacement error S_{2S} up to 70 and 20% of the typical displacement, respectively. Consequently, when one particle displacement is measured, it should be realized there is a relatively large uncertainty in the actual particle velocity. However, because the error is a normal distribution around 0, the standard error in the mean displacement is given as $\hat{\sigma}/\sqrt{N}$, which decreases with increasing number of sampled particles N. The examples in this work focus on velocity distribution in lateral direction. We ensure that for every y-position more than 23,000 particles are measured by increasing the number of frames. The corresponding uncertainty in the velocities is very low ($\approx 0.1\%$), as shown in the last column in Table 2.

Finally, we want to show here how the background can influence the result. As shown in Figure 4, the background can have some bright pixels forming line structures as especially visible near the left wall. This is a consequence of the high magnification which will make it harder for the algorithm to determine the actual velocity. The number of times a certain error occurred at a certain y-position for y and z displacement, is shown in Figure 6. In both cases, the spread in the error near the left wall is slightly larger, however, still centered around 0. Consequently, the measurements are unbiased to the position and are insensitive to a nonsmooth background.

Results and Discussion

Particle position

In Figure 7, examples are shown of 2-D histograms as a function of the particle position in the streamwise (z) and lateral (y) direction. These histograms can be projected on the y axis, yielding a 1-D lateral position PDF as shown in Figure 8. In this figure, the results are shown for different streamwise sections (middle and bottom) and for different superficial gas velocities. The PDF's are averaged over 3 or more datasets; the error bars indicate the standard deviation of this estimator. Before discussing the observed trends, one should first notice that the error bars are sometimes of the same order of magnitude as the difference between different cases. This is mainly important near the walls. A major reason for this is that the different measurements over which is averaged, sometimes do not have their walls at exactly the same position. The shift is only small, about one bin width or 20% of a particle diameter. But a small shift in horizontal direction yields a big difference in histogram height because of the steepness of the graph around the peaks. This introduces a larger standard deviation than one would estimate based on the shapes of the graphs. Furthermore, one should notice that the measured PDF's are symmetric in the sense that peaks are shown on both walls.

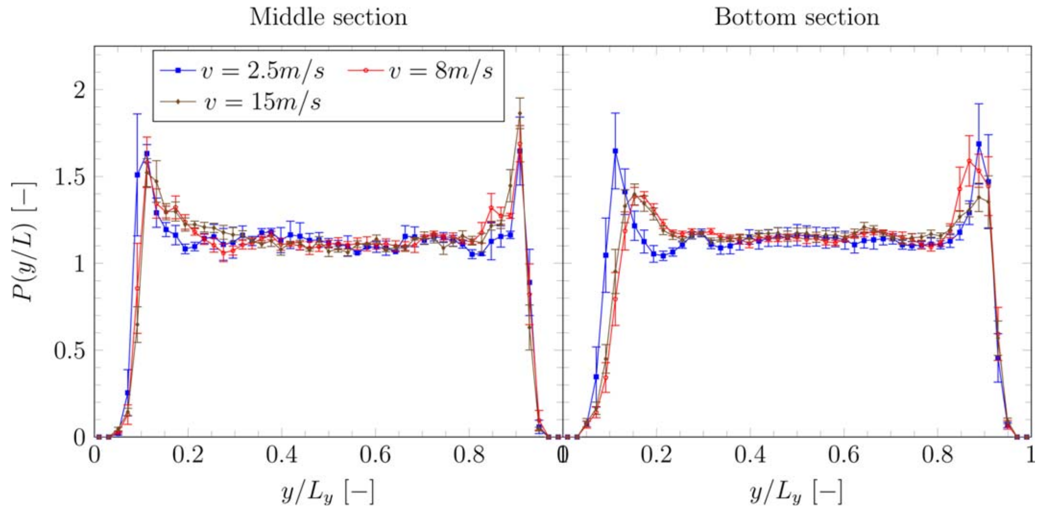

Figure 8. PDF's of the lateral particle position (between two walls) for different gas velocities (see legend).

The left and right figures show the middle and bottom section of the channel, respectively. The error bars indicate the standard deviation of the mean PDF among different datasets. [Color figure can be viewed in the online issue, which is available at wileyonlinelibrary.com.]

However, the shape of the peak is different for the two walls. This asymmetry is partly caused by positioning of the camera, as it is hard to position the camera exactly perpendicular to the duct; even a small declination deteriorates the symmetry. Despite these measurement difficulties, the trends discussed in the following, hold for all cases investigated. This suggests that the observed trends can indeed be attributed to the changes of the operation conditions instead of measurements inaccuracies or random variation around the mean.

The most apparent observation is that peaks are visible near the walls for all cases. Hence, these measurements conclusively show that a particle is more likely to reside near the wall than in the center. Furthermore, with increasing gas velocity the peak becomes lower, broader, and shifts to the center. Both observations are in agreement with Ref. 14 who also measured the particle distribution in a pneumatic conveyed duct. They measured that the particle charge is sufficient to make the particles deposit on the walls if the gas velocity is sufficiently low; otherwise, particle movement is dominated by particle-gas interaction. In our experiments, the electrostatic wall-particle interaction can dominate particle-gas drag because polystyrene is known to acquire electrostatic charge easily. As a matter of fact, the charging of the particles can indeed be measured using this device. However, the

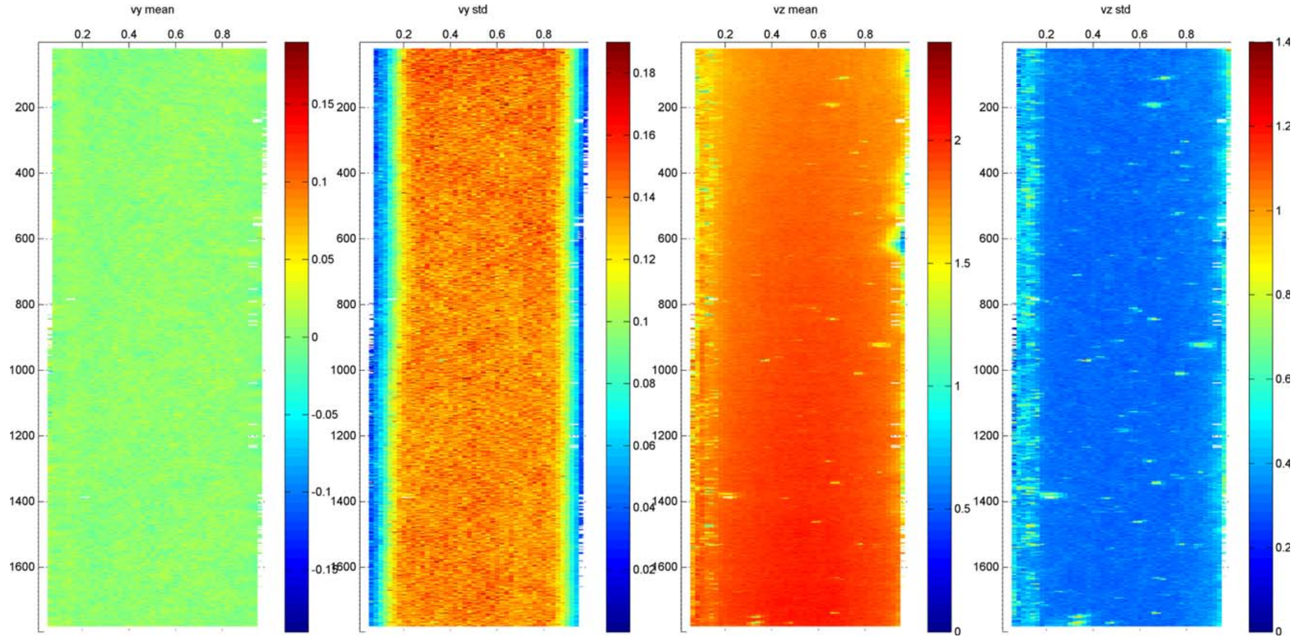

Figure 9. Two-dimensional histograms of the mean and standard deviation of velocity in the lateral (*y*) and streamwise (*z*) direction.

Outer left: mean of v_y; middle left: standard deviation of v_y; middle right: mean of v_z; outer right: standard deviation of v_z. Note that when $v_y>0$ it moves from left to right, and for $v_y<0$ vice versa. The results in this figure are for the lowest gas velocity of 2.5 m/s. [Color figure can be viewed in the online issue, which is available at wileyonlinelibrary.com.]

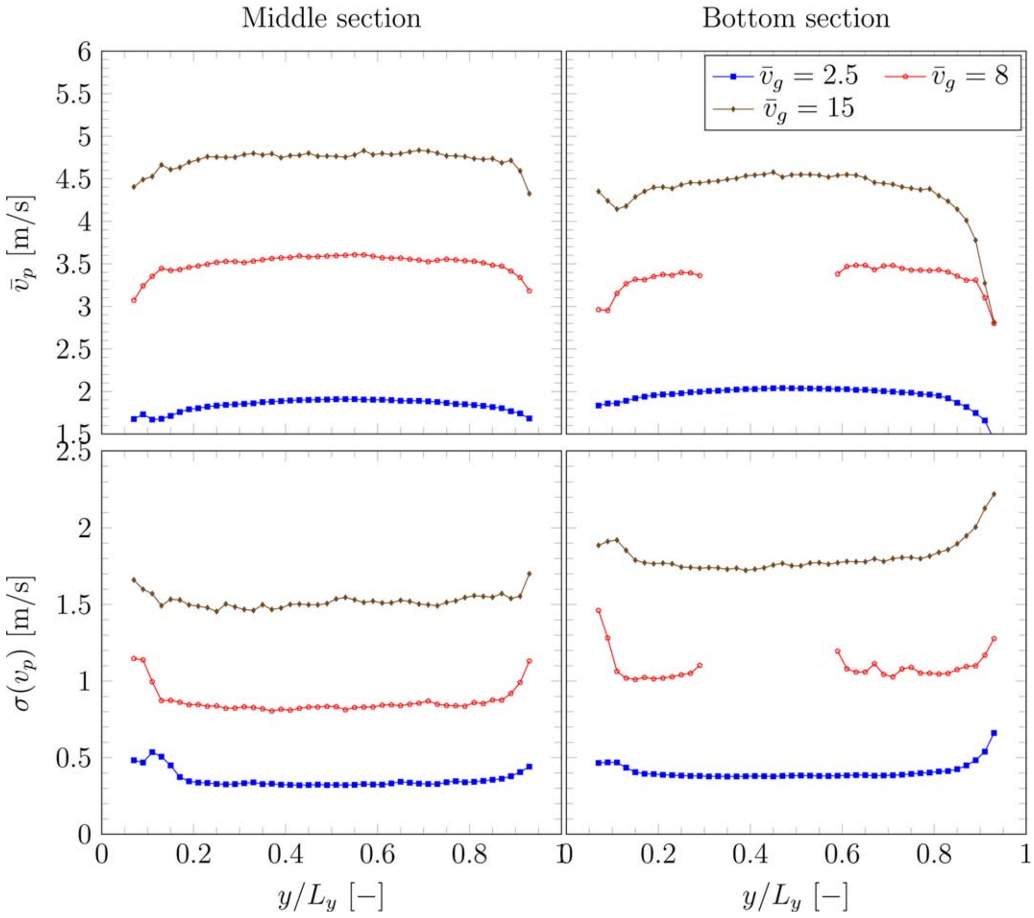

Figure 10. Streamwise particle velocity

The upper and lower rows show the mean and standard deviation of the streamwise velocity (v_z). The left and right columns show the results for the middle and bottom section, respectively. The results are shown where the particle center of mass is more than one particle radius from the wall, $0.13<y/L_y<0.87$. The results for the bottom section with $\bar{v}_g = 8$ m/s are omitted between $0.3 \leq y/L_y \leq 0.575$ because too much fouling occurred at those positions during that experiment.

[Color figure can be viewed in the online issue, which is available at wileyonlinelibrary.com.]

method or results are not shown because it is beyond the scope of this article.

Note that the shift of the peak is much more pronounced in the bottom section. Results of the velocity, as presented in the next subsection, are in agreement with this migration of particles from wall to center.

Velocity

Next, we investigate the spatial distribution of the particle mean velocity. In Figure 9, the 2-D histograms of the particle mean velocity and standard deviation are shown as a function of the (y, z)-position. Note that there is not much difference in the streamwise direction, except for the blue spot at the middle right of the mean streamwise velocity (middle right figure). This blue spot, however, is centered around the place where no or very few particles are detected as illustrated by the PDF of the particles positions in Figure 8. Another observation is that the mean streamwise velocity clearly increases with increasing streamwise position. Furthermore, some speckles are observed in all four plots; these are positions where the algorithm suffers from background features.

The 2-D histograms can be projected to the y axis, as was also done for the spatial position PDF. Such a projection will average out the erroneous speckles discussed above. The results are shown for the mean and standard deviation of the streamwise velocity in Figure 10 for different gas velocities and streamwise sections (middle and bottom). For all cases, it is observed that the mean streamwise particle velocity is flat in the center and decreases slightly toward the walls.

Another observation is that the particle velocity increases with gas velocity. For the lowest gas velocity, the particles reach almost the superficial gas velocity for all cases. However, if the superficial gas velocity is increased, to 8 or 15 m/s, particles only reach a velocity of 3–4 or 5–6 m/s, respectively. At first sight, this could be explained by comparing the particle Stokes relaxation time, which for our particles is equal to $\tau_{St}=\rho_p D_p^2/(18\mu_g)=0.49$ s, against the residence time in the duct, which is equal to $\tau_r=L_z/\bar{v}_{p,z}=0.1$ s if the lowest gas velocity (2.5 m/s) is taken as the averaged particle velocity. So even for the lower velocity of 2.5 m/s, we have $\tau_r < \tau_{St}$, and consequently the particle will not fully reach the superficial gas velocity. This analysis implies that the particle velocity will keep increasing with streamwise position until the particle exits the duct or the superficial gas velocity is reached. This is true for the lower gas velocity. However, at the two higher gas velocities the particle velocity does not increase between the middle and bottom section, and even decreases a little. In this article, we focus on the PIV/PTV method development, and

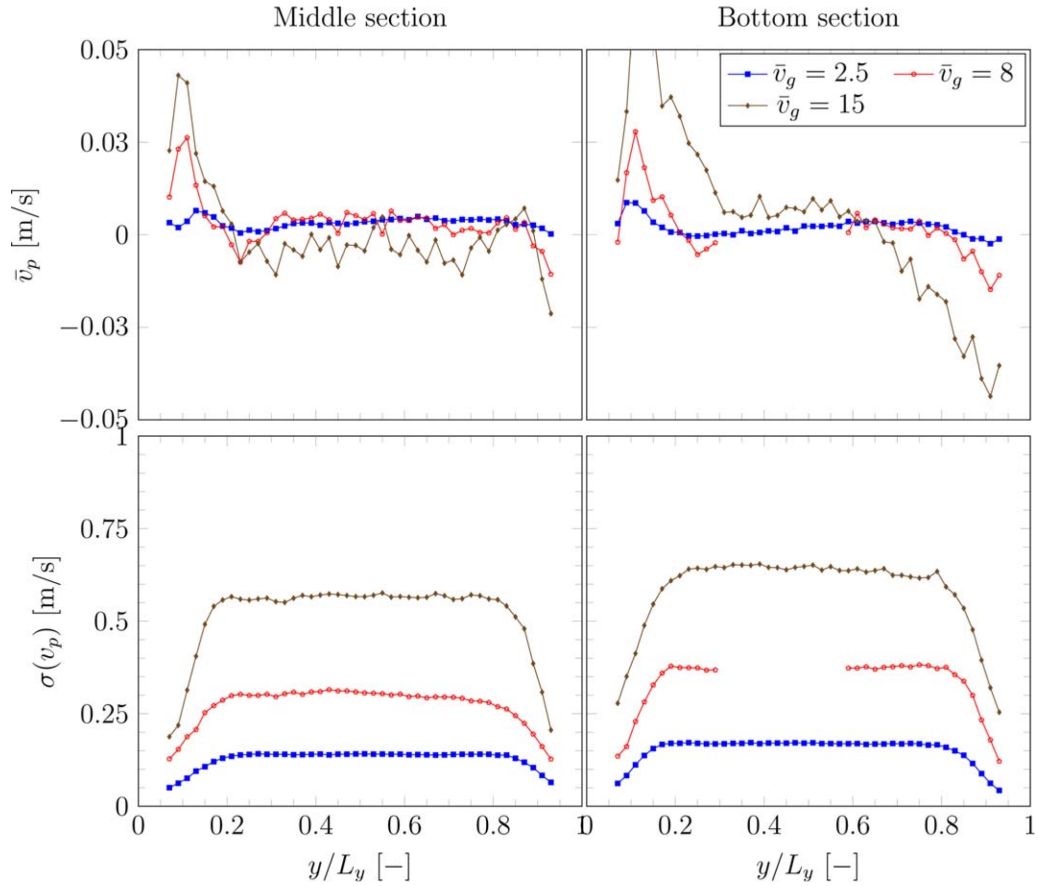

Figure 11. Same as Figure 10, but now for the lateral velocity (v_y).

Note that when v_y>0 it points from the left to right wall, when v_y<0 from right to left wall, which is the case at the left and right wall, respectively. The lateral velocity is consequently pointing toward the centers at both walls.

[Color figure can be viewed in the online issue, which is available at wileyonlinelibrary.com.]

therefore decided to refrain from the full analysis and explanation of this seemingly surprising effect. This is possibly caused by the particle charging; we can go in more detail in a forthcoming paper, where we will compare these measurements with a detailed discrete particle computer simulation model.

In the bottom row of Figure 10, the standard deviation of the streamwise velocity is shown. In all cases, the standard deviation is constant in the center and increases toward the walls. This is stronger for the lower mass rate, especially in the lower section (lower left figure). The increase in standard deviation near the walls can partly be explained by the intrinsic spread in the standard deviation within one bin; the streamwise velocity profile is steepest near the wall and decreases toward the center.

In Figure 11, the mean and standard deviation of the velocity in the lateral direction is shown. In all cases, the velocity is 0 in the center, while it is positive at the left wall and negative at the right; this increases with increasing gas velocity. Hence the particles have an increasing velocity toward the center at both walls with increasing gas velocity. Consequently, there must be a net migration of particles away from the walls which is more pronounced at high gas velocity. Also, note that this migration is fully consistent with the decrease of the near-wall peak observed in the spatial PDF's in Figure 8. This migration phenomenon can be caused by the still developing flow as this yields a flow of the gas to the center. In case of single-phase flow with a flat, irrotational inflow profile, the boundary layer thickness δ grows as $\delta = \sqrt{2\mu_g t/\rho_g} \approx \sqrt{2\mu_g z/(\rho_g v_{bg})}$ with t the time elapsed since the fluid has entered the duct which can be approximated as $t \approx z/v_{bg}$ if we assume that the gas velocity in the core region will not differ too much from the superficial gas velocity. For $v_{bg} = 8$ m/s and $v_{bg} = 15$ m/s, this yields a boundary layer thickness of 1 and 0.7 mm, respectively, at the end of the duct. Conversely, for $v_{bg} = 2.5$ m/s the flow has fully developed after a streamwise distance of approximately 70 mm. Furthermore, there is a gradient of the streamwise velocity in y-direction and the particles are moving slower than the gas. Hence a lift force pointing from the walls is exerted on the particles. As this gradient will be larger for higher gas velocities, the lift force will increase. Again, we defer a full explanation to a forthcoming paper.

Finally, we will discuss the standard deviation of the lateral velocity of the particles as shown in Figure 11. This quantity is a measure for the absolute magnitude of the velocities in lateral direction. In all cases, it is flat in the center and decreases toward the walls. Note that this is qualitatively different from the standard deviation of the streamwise velocity, which increases toward the walls. The decrease of the particle lateral velocity near the walls might be caused by the lubrication force. This force describes the dramatic increase of the drag when a particles' distance to the wall becomes smaller than a its diameter. Indeed, the standard deviation starts to decrease when the center of the particle is of this order of magnitude, at $1.5D_p = 0.2L_y$.

Conclusions

In this article, we developed a method to determine the distribution of particle positions and average particle velocities accurately in two phase gas–solid flows through small, narrow channels. This is achieved using a Hough transform to acquire the positions and PIV for the particle velocity, using an interrogation area of one particle diameter. The latter is possible because here the particle image contains two bright spots, which are the glare points caused by the two frontal positioned lights.

This hybrid PIV-PTV method will outperform PTV if the segmentation of the particles is a problem: PTV strongly depends on the detection of particles, while this method does not. Such particle segmentation problems can occur when lighting is poor, contrast between particle and background is low, or the background is feature rich. It should be noted that PTV is computationally less demanding than the method proposed in this article. Moreover, for PTV the interframe displacement can be a large fraction of the nearest neighbor distance, while for our method the interframe displacement should be less than the interrogation area because just as with normal PIV the particle should not leave the interrogation area in between two frames. For dilute flows, this leads to requirement of a higher frame rate of the images in our method compared to standard PTV.

Compared to PIV, our hybrid method has the benefit that it will work with a much lower source density, as for example found in pneumatic conveying. Furthermore, it allows a much higher spatial resolution of the mean particle velocity, than PIV because the velocity of individual particles is determined instead of the ensemble of particles inside an interrogation area of a few particle diameters large. This is desirable when one wants to investigate the velocity development over a distance smaller than the size of an individual particle. This is often the case when the particles are large compared to the dimensions of the confining geometry, as is the case in the examples shown in this article. If the flow is so dense that multiple particles reside in the interrogation area, the hybrid PIV-PTV method will break down as it will be impossible to determine individual particle velocities. In such a case, it is better to use PIV instead.

In summary, the hybrid PIV-PTV method is applicable at any scale where PTV is not feasible due to difficulties in segmentation of the particles or PIV is not feasible because the required resolution of the velocity distribution is less than a particle diameter.

In this article, the hybrid PIV-PTV method has been applied to a system where particle velocities up to 8 m/s were measured while the illumination was done with LED. The PDF of lateral particle position was measured, together with the mean streamwise and lateral velocity. It was shown that in this system particles tend to be closer to the wall and that this effect decreases with increasing superficial gas velocity. Furthermore, it was shown that the particles have a higher velocity with increasing superficial gas velocity. The third quantity shown was the mean lateral particle velocity as function of its lateral position. The lateral velocity is 0 in all cases, except for particles near the wall, for which the average velocity pointed away from either wall and increased with increasing gas velocity. This is in agreement with the decreasing near-wall peaks of the spatial PDF with increasing gas velocity. The last illustrative result shown was the standard deviation of the lateral particle velocity as function of particle lateral position. It was shown that the standard deviation increases with increasing gas velocity and is smaller near the walls than in the center of the channel. In the discussion, some speculations on the reasons for all these observations are given.

Outlook

Now the method to determine particle positions and velocities has been demonstrated, research on the results can be performed to understand the system behavior. In future work, these results will be related to measurements of the amount of charge the particles acquire. Furthermore, a more detailed study on the system will be performed using a numerical approach using DEM-CFD. The measured quantities as presented in this work can also be acquired using DEM-CFD and therefore constitutes an excellent dataset to validate the DEM-CFD model.

Acknowledgments

This research is supported by the Dutch Technology Foundation STW, which is part of the Netherlands Organization for Scientific Research (NWO) (project number 11399). Additional support is obtained from the Institute for Sustainable Process Technology, ISPT. Furthermore, the authors thank the European Research Council for funding the used camera (contract numbers 247298 and 259521).

Literature Cited

1. Fokeer S, Kingman S, Lowndes I, Reynolds A. Characterisation of the cross sectional particle concentration distribution in horizontal dilute flow conveying - a review. *Chem Eng Process.* 2004;43(6): 677–691.
2. Laín S, Sommerfeld M. Numerical calculation of pneumatic conveying in horizontal channels and pipes: detailed analysis of conveying behaviour. *Int J Multiphase Flow.* 2012;39:105–120.
3. Sommerfeld M, Ho CA. Numerical calculation of particle transport in turbulent wall bounded flows. *Powder Technol.* 2003; 131(1):1–6.
4. Jones MG, Williams KC. Predicting the mode of flow in pneumatic conveying systems – a review. *Particuology.* 2008;6(5):289–300.
5. Zhou F, Hu S, Liu Y, Liu C, Xia T. CFD – DEM simulation of the pneumatic conveying of fine particles through a horizontal slit. *Particuology.* 2014;16:196–205.
6. Higashiyama Y, Asano K. Recent progress in electrostatic separation technology. *Part Sci Technol.* 1998;16(1):77–90.
7. Matsusaka S, Maruyama H, Matsuyama T, Ghadiri M. Triboelectric charging of powders: a review. *Chem Eng Sci.* 2010;65(22):5781–5807.
8. Schutyser MAI, van der Goot AJ. The potential of dry fractionation processes for sustainable plant protein production. *Trends Food Sci Technol.* 2011;22(4):154–164.
9. Hemery Y, Holopainen U, Lampi AM, Lehtinen P, Nurmi T, Piironen V, Edelmann M, Rouau X. Potential of dry fractionation of wheat bran for the development of food ingredients, part II: electrostatic separation of particles. *J Cereal Sci.* 2011;53(1):9–18.
10. Wang J, de Wit M, Schutyser MAI, Boom RM. Analysis of electrostatic powder charging for fractionation of foods. *Innov Food Sci Emerg Technol.* 2014;26:360–365.
11. Wang H, Chen S, Cai B, Ge L, Chen Q. Study on the dynamics of tribocharged coal and mineral particles in free-fall triboelectric separator. *Sep Sci Technol.* 2014;49(18):2990–2998.
12. Pelgrom PJM, Vissers AM, Boom RM, Schutyser MAI. Dry fractionation for production of functional pea protein concentrates. *Food Res Int.* 2013;53(1):232–239.
13. Zheng Y, Liu Q. Review of techniques for the mass flow rate measurement of pneumatically conveyed solids. *Measurement.* 2011;44(4):589–604.

14. Yao J, Zhang Y, Wang CH, Liang YC. On the electrostatic equilibrium of granular flow in pneumatic conveying systems. *AIChE J*. 2006;52(11):3775–3793.
15. Harper WR. The volta effect as a cause of static electrification. *Proc R Soc London Ser A Math Phys Sci*. 1951;205(1080):83–103.
16. Wang J, Smits E, Boom R, Schutyser M. Arabinoxylans concentrates from wheat bran by electrostatic separation. *J Food Eng*. 2015;155:29–36.
17. Lindken R, Rossi M, Grosse S, Westerweel J. Micro-particle image velocimetry (microPIV): recent developments, applications, and guidelines. *Lab Chip*. 2009;9(17):2551–2567.
18. Fiscaletti D, Westerweel J, Elsinga GE. Long-range μPIV to resolve the small scales in a jet at high Reynolds number. *Exp Fluids*. 2014;55(9):1812.
19. Hagsaeter SM, Westergaard CH, Bruus H, Kutter JP, Hagsäter SM. Investigations on LED illumination for micro-PIV including a novel front-lit configuration. *Exp Fluids*. 2007;44(2):211–219.
20. Westerweel J. Fundamentals of digital particle image velocimetry. *Meas Sci Technol*. 1997;8(12):1379–1392.
21. Adrian RJ. Scattering particle characteristics and their effect on pulsed laser measurements of fluid flow: speckle velocimetry vs particle image velocimetry. *Appl Opt*. 1984;23(11):1690–1691.
22. Atherton TJ, Kerbyson DJ. Size invariant circle detection. *Image Vis Comput*. 1999;17(11):795–803.
23. Yuen HK, Princen J, Illingworth J, Kittler J. Comparative study of Hough transform methods for circle finding. *Image Vis Comput*. 1990;8(1):71–77.

Manuscript received Feb. 2, 2015, and revision received May 19, 2015.